

# 1 An analysis of superhydrophobic turbulent drag reduction mechanisms 2 using direct numerical simulation

3 Michael B. Martell, Jonathan P. Rothstein, and J. Blair Perot<sup>a)</sup>

4 *Department of Mechanical and Industrial Engineering, University of Massachusetts Amherst,*  
5 *Amherst, Massachusetts 01003, USA*

6 (Received 26 October 2009; accepted 22 April 2010; published online xx xx xxxx)

7 Superhydrophobic surfaces combine hydrophobic surface chemistry with topological microfeatures.  
8 These surfaces have been shown to provide drag reduction in laminar and turbulent flows. In this  
9 work, direct numerical simulation is used to investigate the drag reducing performance of  
10 superhydrophobic surfaces in turbulent channel flow. Slip velocities, wall shear stresses, and  
11 Reynolds stresses are determined for a variety of superhydrophobic surface microfeature geometry  
12 configurations at friction Reynolds numbers of  $Re_\tau \approx 180$ ,  $Re_\tau \approx 395$ , and  $Re_\tau \approx 590$ . This work  
13 provides evidence that superhydrophobic surfaces are capable of reducing drag in turbulent flow  
14 situations by manipulating the laminar sublayer. For the largest microfeature spacing, an average  
15 slip velocity over 80% of the bulk velocity is obtained, and the wall shear stress reduction is found  
16 to be greater than 50%. The simulation results suggest that the mean velocity profile near the  
17 superhydrophobic wall continues to scale with the wall shear stress and the log layer is still present,  
18 but both are offset by a slip velocity that is primarily dependent on the microfeature spacing.

19 © 2010 American Institute of Physics. [doi:10.1063/1.3432514]  
20

## 21 I. BACKGROUND

22 Superhydrophobic surfaces are characterized by both  
23 chemical hydrophobicity and microscale topological rough-  
24 ness. The most overt physical characteristic of these surfaces  
25 is that water droplets bead on them with high contact angles  
26 (up to  $179^\circ$ ) so that the droplets are very nearly spherical.<sup>1-3</sup>  
27 These contact angles are much higher than those obtained by  
28 purely chemical surface treatments which achieve maximum  
29 contact angles of about  $130^\circ$ . Nearly spherical droplets roll  
30 very easily when the surface is tilted or moved. It is believed  
31 that lotus leaves (which have a superhydrophobic surface)  
32 take advantage of this effect to be self-cleaning.<sup>3</sup> The rolling  
33 droplets pick up dust and dirt particles as they roll off of the  
34 leaf.

35 The ease with which water droplets move on superhy-  
36 drophobic surfaces prompted researchers to consider if such  
37 surfaces might also reduce drag in pipe and channel flow.  
38 Early experiments<sup>4-8</sup> suggested that they did indeed reduce  
39 drag in both laminar and turbulent boundary layer flows.  
40 However, the reasons for this apparent drag reduction were  
41 not clear, as the mechanisms at work in droplet motion can-  
42 not be present in these flows. Leading and trailing contact  
43 angles certainly have no role in channel or pipe flow. The  
44 explanation for superhydrophobic drag reduction in laminar  
45 channels was first demonstrated in Ou *et al.*<sup>9</sup> In short, it was  
46 shown that air trapped in the microscale features is respon-  
47 sible for drag reduction. For a normal hydrophilic surface,  
48 capillary (surface tension) forces would quickly drive air out  
49 of the small surface cavities (as occurs in a sponge or cloth).  
50 However, because the surface is also chemically hydropho-  
51 bic, the water resists being drawn into the microcavities. As

a result, superhydrophobic surfaces trap air at their surface<sup>52</sup>  
and may even be able to remove dissolved air from the water<sup>53</sup>  
solution. Beyond its role in allowing air cavities to form,<sup>54</sup>  
chemical hydrophobicity has little or no effect on the subse-<sup>55</sup>  
quent drag reduction. Drag reduction results from the fact<sup>56</sup>  
that water can slip over the air cavity surface, whereas it<sup>57</sup>  
comes to rest on a flat solid surface, hydrophobic or not.<sup>58</sup>

The amount of drag reduction in laminar flows is prima-<sup>59</sup>  
rily a function of the size of the air cavities; increasing the<sup>60</sup>  
fraction of air on the surface or increasing the spacing of the<sup>61</sup>  
features increases the slip and the drag reduction.<sup>9,10</sup> The<sup>62</sup>  
maximum size of the air cavities is limited by the fact that<sup>63</sup>  
air-water interfaces bridging very large cavities can fail. This<sup>64</sup>  
occurs when the pressure becomes large enough to over-<sup>65</sup>  
whelm the surface tension forces supporting the cavity or<sup>66</sup>  
when gravitational, shear, or other dynamic instabilities are<sup>67</sup>  
strong enough to rupture the air cavity's free surface. Subse-<sup>68</sup>  
quent research efforts<sup>10-12</sup> have confirmed this model of<sup>69</sup>  
laminar drag reduction due to superhydrophobic surfaces. In<sup>70</sup>  
the case of roughness composed of regularly spaced ridges<sup>71</sup>  
an analytical solution corresponding to this model exists<sup>13-15</sup>  
and experimental results appear to agree well with this<sup>72</sup>  
solution,<sup>9,10</sup> specifically velocity profiles above the no-slip<sup>73</sup>  
and shear-free regions of the surfaces discussed in Philip<sup>13,14</sup>  
and Lauga.<sup>15</sup><sup>74</sup>  
<sup>75</sup>  
<sup>76</sup>

Most research on superhydrophobic surfaces currently<sup>77</sup>  
involves very regular surface geometries—often regularly<sup>78</sup>  
spaced ridges or posts. These surfaces tend to be used in<sup>79</sup>  
research as they allow very precise characterization of the<sup>80</sup>  
topology. The model suggests that surface topology is the<sup>81</sup>  
primary factor in the resultant drag reduction thus it is im-<sup>82</sup>  
portant to characterize. This paper will continue in the tradi-<sup>83</sup>  
tion of using simple, easily characterized surfaces, but it<sup>84</sup>

<sup>a)</sup>Electronic mail: perot@ecs.umass.edu.

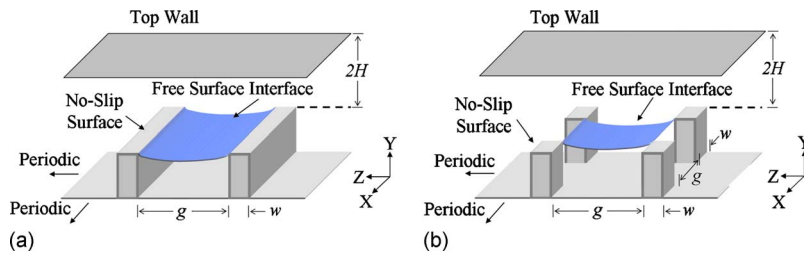


FIG. 1. (Color online) Schematic of geometry and relevant dimensions for superhydrophobic surface features. Note that in the simulations, the air-water interface is flat.

should be noted that in practice unstructured surface roughness works just as well, and is often easier to fabricate. Some early experiments<sup>16</sup> used plasma etched polypropylene which produces a random surface that achieved up to 25% drag reduction. More recent experiments have used hydrophobically treated sand paper.<sup>17</sup>

The use of superhydrophobic surfaces to produce laminar drag reduction in boundary layers is interesting since, at millimeter scales, no other drag reduction process is known. At nanoscales, chemical slip is possible and electrostatic effects are possible. On the other hand, for turbulent boundary layer flows there are numerous and quite varied ways to achieve drag reduction. These include fluid additives such as polymers and air bubbles,<sup>18</sup> surface modifications such as riblets,<sup>19</sup> compliant coatings,<sup>20</sup> and active control techniques. Work by Tyrrell and Attard<sup>21</sup> investigated the role of nanobubbles trapped in hydrophobic surfaces and their relation to drag reduction. However, given the huge variety of different kinds of turbulent boundary layer applications, it is of interest to also understand the drag reducing properties and controlling mechanisms of superhydrophobic surfaces on turbulent boundary layers.

In a typical boundary layer, surface roughness enhances the turbulence levels and the drag. It is therefore not entirely obvious that superhydrophobic surfaces (and their associated surface roughness) will necessarily reduce drag in a turbulent boundary layer. Nevertheless, early experiments<sup>4,8</sup> indicated that drag reduction does occur when using superhydrophobic

surfaces even for turbulent flows. More recent experiments<sup>22,23</sup> have confirmed this. A theoretical analysis by Fukugata<sup>24</sup> proposes an explanation of how a small alteration of the laminar sublayer can affect the entire turbulent boundary layer and subsequently alter the drag.

Perhaps the earliest computational study of these surfaces was performed by Min and Kim.<sup>25,26</sup> This was a turbulent channel flow simulation in which an assumed slip boundary condition was applied and drag reduction was observed. The slip boundary condition is an effective (macroscopic) boundary condition, not a physical one, so these simulations correspond to the situation where the spacing of the surface roughness elements is much smaller than any turbulent eddies. Martell *et al.*<sup>27</sup> performed direct numerical simulations in which the topology was fully resolved at a single Reynolds number  $Re_\tau \approx 180$ . This means that no-slip boundary conditions were imposed on the roughness elements (posts or ridges) and a pure slip (no stress) boundary condition was imposed at the air cavity interface. The effective macroscopic slip of the surfaces was then calculated from the simulation, not imposed by it. The simulations in our previous work<sup>27</sup> had a roughness feature spacing that was of a size comparable to the energetic near-wall vortex size and streak spacing.

In Martell *et al.*,<sup>27</sup> the effects of superhydrophobic surface spacing and geometry were studied at a single turbulent Reynolds number. An increase in slip velocity and drag re-

TABLE I. Reynolds numbers, line types, geometric ratios, and length scales for the cases investigated. Note that most  $Re_\tau \approx 180$  cases are presented in Martell *et al.* (Ref. 27).

$Re_\tau$	Line type	Geometry	$g/w$	$w/H$	$g/H$	$w^+$	$g^+$
180	...	Ridges	1.0	0.093 75	0.093 75	16.875	16.875
			1.0	0.187 50	0.187 50	33.750	33.750
			1.6	0.140 62	0.234 36	25.312	42.187
		Posts	3.0	0.093 75	0.281 24	16.875	50.625
			1.0	0.187 50	0.187 50	33.750	33.750
			1.6	0.140 62	0.234 36	25.312	42.187
	...	Transverse ridges	3.0	0.093 75	0.281 24	16.875	50.625
			1.0	0.187 50	0.187 50	33.750	33.750
395	...	Ridges	1.0	0.093 75	0.093 75	37.031	37.031
			1.0	0.187 50	0.187 50	74.062	74.062
		Posts	3.0	0.093 75	0.281 24	37.031	111.09
590	...	Ridges	1.0	0.187 50	0.187 50	110.62	110.62
		Posts	3.0	0.093 75	0.281 24	55.313	165.94

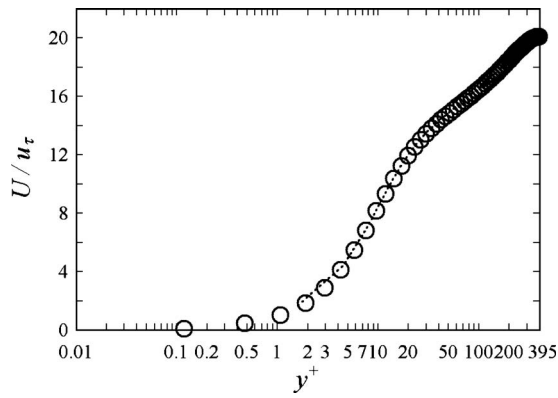


FIG. 2.  $Re_\tau \approx 395$ . A comparison of near wall velocity profiles obtained from Moser *et al.* (Ref. 30) ( $\circ$ ) and the CFD code ( $\cdots$ ) for turbulent channel flow between two infinite parallel plates.

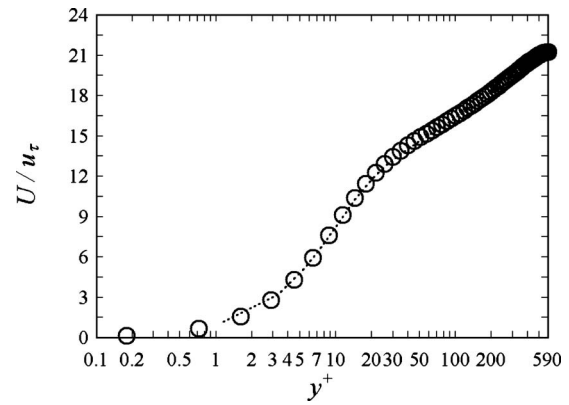


FIG. 4.  $Re_\tau \approx 590$ . A comparison of near wall velocity profiles obtained from Moser *et al.* (Ref. 30) and the CFD code (see Fig. 2 for symbol key).

duction with increasing feature spacing and increased free surface area were observed. The Reynolds stresses showed a marked shift with the presence of a superhydrophobic surface.  $R_{11}$ ,  $R_{22}$ , and  $R_{33}$  curves peaked lower and closer to the superhydrophobic surface than their smooth channel counterpart. The shear stress  $R_{12}$  shifted toward the superhydrophobic wall. This paper is a continuation of Martell *et al.*<sup>27</sup> that explores the effect of Reynolds number on superhydrophobic surface performance, as well as the effect of larger roughness spacing, and the underlying physical processes responsible for the turbulent boundary layer drag reduction.

## II. COMPUTATIONAL APPROACH

The two roughness configurations considered in this work are shown in Fig. 1. In both configurations turbulent channel flow with a constant pressure gradient is simulated. The flow has periodic boundary conditions applied in the streamwise ( $X$ ) and spanwise ( $Z$ ) directions. A regular, no-slip wall is applied at the top of the channel, and regions of no-slip (on the top of the ridge or post) and pure slip flow (on the air cavity interface) are applied on the superhydrophobic lower wall. Only the water side of the air cavity is simulated, and the free surface between the posts or ridges is assumed to be perfectly flat. Recent work by Ybert *et al.*<sup>28</sup> suggests

that curvature effects exist, but have a negligible effect on the drag under modest static pressures. Estimates based on the maximum possible deflection angle of  $12^\circ$  (Ref. 29) also suggest curvature is a secondary influence. The assumption of a pure slip surface at the air interface is reasonable if the roughness features are tall enough (i.e., the same order of magnitude as the spacing). Very thin air cavities could lead to shear flow in the air cavities and a deviation from the slip boundary condition at the air cavity free surface.

The dimensionless length of the channel was  $L_x/H=6$  where  $H$  is the channel half height. The width was  $L_z/H=3$ . This is roughly equivalent to the values of  $2\pi$  and  $\pi$  that were found to be sufficient for prior spectral simulations of channel flow.<sup>30</sup> The simulations do not require dimensions, but for comparison with experiments we note that if the working fluid was water (at  $20^\circ\text{C}$ ), these computations correspond to a channel half height  $H$  on the order of  $0.15\text{ mm}$  if the post or ridge sizes are assumed to be  $30\text{ }\mu\text{m}$  across (which is a common size found in experiments<sup>22,31</sup>). A total of 13 cases were simulated. They are described in Table I. At higher Reynolds numbers this study looks at equally spaced ridges (50% free surface area), and widely spaced posts (93.75% free surface area). In addition, a case with evenly spaced ridges perpendicular to the flow direction at  $Re_\tau \approx 180$ , referred to as transverse ridges, was investigated.

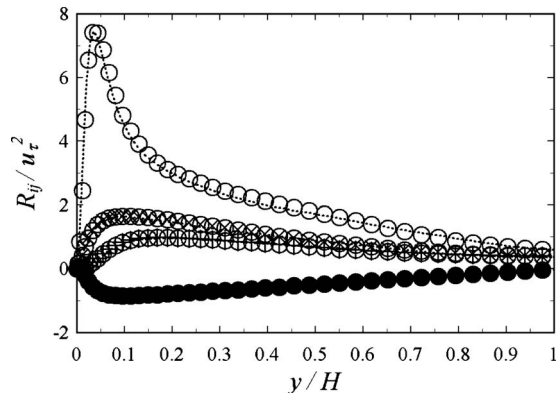


FIG. 3.  $Re_\tau \approx 395$ . A comparison of Reynolds stress profiles obtained from Moser *et al.* (Ref. 30) ( $\circ$   $R_{11}$ ,  $\oplus$   $R_{22}$ ,  $\otimes$   $R_{33}$ ,  $\bullet$   $R_{12}$ ) and the CFD code ( $\cdots$ ) for turbulent channel flow between two infinite parallel plates.

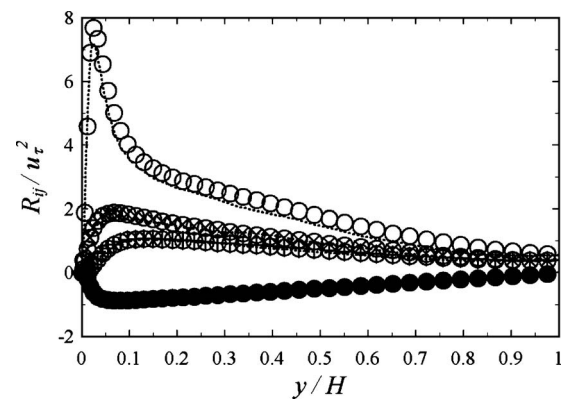


FIG. 5.  $Re_\tau \approx 590$ . A comparison of Reynolds stress profiles obtained from Moser *et al.* (Ref. 30). See Fig. 3 for symbol key.

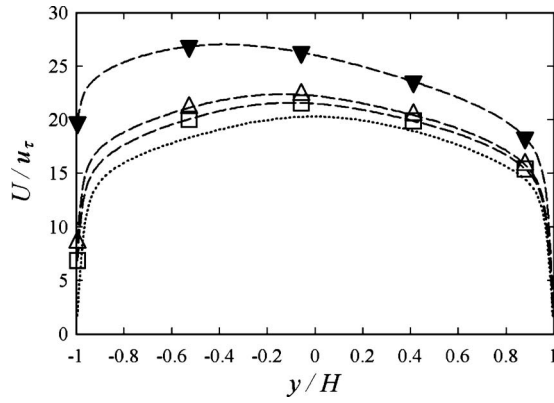


FIG. 6.  $Re_\tau \approx 395$ . Velocity profiles from simulations with  $w^+ = g^+ = 37.031$  ( $\square$ ) and  $w^+ = g^+ = 74.062$  ( $\triangle$ ) ridges, as well as  $w^+ = 37.031$  and  $g^+ = 111.09$  ( $\blacktriangledown$ ) posts. Regular channel profile ( $\cdots$ ) shown for reference. Note that symbols are used to identify curves, and do not reflect data point locations.

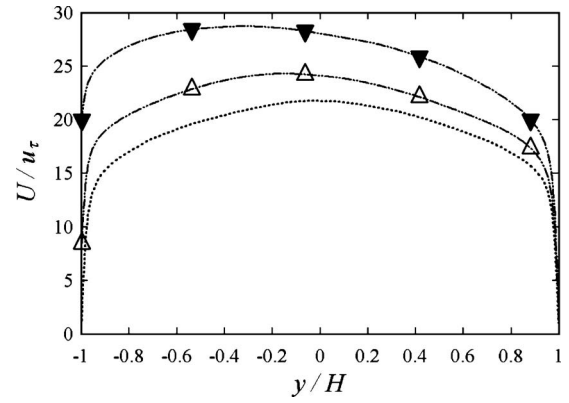


FIG. 8.  $Re_\tau \approx 590$ . Velocity profiles from simulations with  $w^+ = g^+ = 110.62$  ( $\triangle$ ) ridges, as well as  $w^+ = 55.313$  and  $g^+ = 165.94$  ( $\blacktriangledown$ ) posts. Regular channel profile ( $\cdots$ ) shown for reference. Note that symbols are used to identify curves, and do not reflect data point locations.

188 The  $Re_\tau \approx 180$  cases use  $128^3$  grid points for each simu-  
 189 lation. The  $Re_\tau \approx 395$  cases require  $256^3$  grid points, and the  
 190  $Re_\tau \approx 590$  cases use  $512^3$  grid points per simulation. A uni-  
 191 form mesh is employed in all directions. Stretching in the  
 192 wall normal direction is not required. The code uses a stag-  
 193 gered mesh spatial discretization, low-storage third-order  
 194 Runge–Kutta time advancement for the advection terms,  
 195 trapezoidal advancement for the viscous terms, and a classic  
 196 fractional step method for the pressure term and incompress-  
 197 ibility constraint.<sup>32</sup> It is parallelized using MPI libraries and  
 AQ: 198 efficiently hides all inter-CPU data transfers by performing  
 #1 199 them asynchronously during the computations. The spatial  
 200 discretization has no artificial dissipation associated with it<sup>33</sup>  
 201 (which could alter the turbulent energy cascade<sup>34</sup>). The nu-  
 202 merical method locally conserves vorticity (or circulation),  
 203 as well as mass and momentum, to machine precision.<sup>35</sup>  
 204 The code has been extensively tested.<sup>27,29,36,37</sup> It was  
 205 validated for laminar superhydrophobic surface calculation  
 206 and turbulent superhydrophobic surfaces at  $Re_\tau \approx 180$  in  
 207 Martell *et al.*<sup>27</sup> Validation of the turbulence simulation capa-  
 208 bilities of the code against the higher Reynolds number stan-  
 209 dard channel flow simulations of Moser *et al.*<sup>30</sup> are shown in  
 210 Figs. 2–5. These figures show the mean flow and Reynolds  
 211 stresses that are computed when the bottom wall is a regular

no-slip wall. Only half of the domain is shown since the  
 statistics are symmetric for this particular case. The mean  
 flow matches to within 2% and the Reynolds stresses match  
 to within 5%. The greatest difference is in the stream-  
 wise Reynolds stress in the core of the channel. Streamwise  
 and spanwise velocity correlations were also calculated for  
 all three regular no-slip wall benchmark cases ( $Re_\tau \approx 180$ ,  
 $Re_\tau \approx 395$ , and  $Re_\tau \approx 590$ ). Correlations approached zero  
 as the edge of the computational domain was reached, and  
 generally agreed with correlation data provided by Moser  
*et al.*,<sup>30</sup> although temporal averaging was not employed. Cor-  
 relation data for the regular wall  $Re_\tau \approx 395$  case is compared  
 with streamwise and spanwise velocity correlations from a  
 case with widely spaced posts in Sec. V, Figs. 39 and 40.  
 These figures show that the size of the computational domain  
 is sufficient not only for a regular wall channel but also when  
 significant slip is present on the bottom wall. This is dis-  
 cussed further in Sec. V. In addition to comparisons with  
 Moser *et al.*,<sup>30</sup> a mesh resolution study was performed. This  
 simulation involved evenly spaced ridges (with  $g/w = 1$ ) at  
 $Re_\tau \approx 180$ . This simulation was run with both  $128^3$  and  $256^3$   
 meshes. The Reynolds stresses were all within 3% of each  
 other, and the mean velocity profiles differ by less than 0.5%  
 of the bulk velocity.

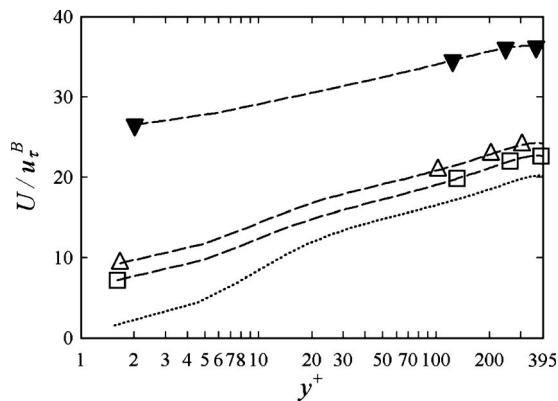


FIG. 7.  $Re_\tau \approx 395$ . A closer look at velocity profiles from Fig. 6, using the local friction velocity,  $u_\tau^B$ , to normalize the velocity and calculate  $y^+$ .

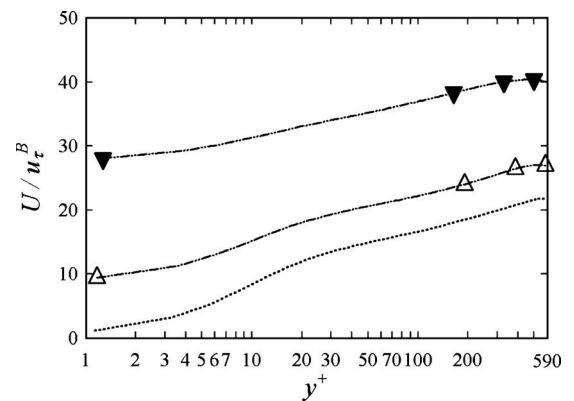


FIG. 9.  $Re_\tau \approx 590$ . A closer look at velocity profiles from Fig. 8, using the local friction velocity  $u_\tau^B$  to normalize the velocity and calculate  $y^+$ .



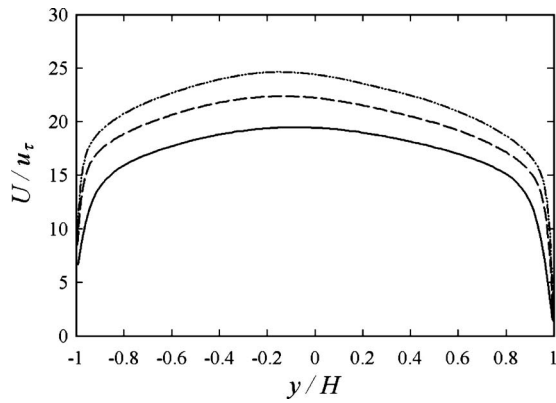


FIG. 10. Comparison of velocity profiles for  $g/w=1$ ,  $w/H=g/H=0.1875$  ridges across the three Reynolds numbers investigated:  $Re_\tau \approx 180$  (—) with  $w^+=g^+=33.75$ ,  $Re_\tau \approx 395$  (---) with  $w^+=g^+=74.062$ , and  $Re_\tau \approx 590$  (-·-·-) with  $w^+=g^+=110.62$ .

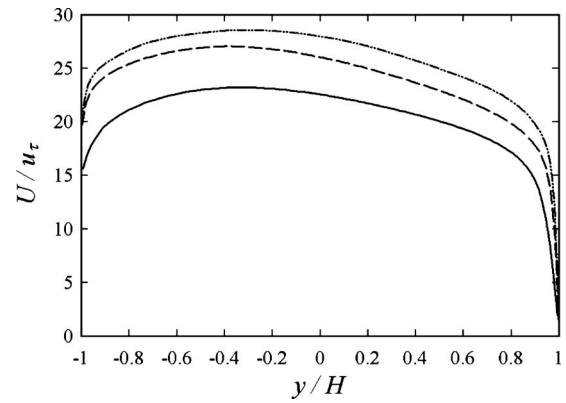


FIG. 12. Comparison of velocity profiles for  $g/w=3$ ,  $w/H=0.09375$ ,  $g/H=0.28124$  posts across the three Reynolds numbers investigated:  $Re_\tau \approx 180$  (—) with  $w^+=16.875$ ,  $g^+=50.625$ ;  $Re_\tau \approx 395$  (---) with  $w^+=37.031$ ,  $g^+=111.09$ ; and  $Re_\tau \approx 590$  (-·-·-) with  $w^+=55.313$ ,  $g^+=165.94$ .

### 236 III. MEAN FLOW

237 In the case of the ridge topology, the ridges are always  
 238 aligned with the mean flow (except in the special case of  
 239 transverse ridges), thus the turbulent statistics depend on  
 240 both the distance from the surface ( $Y$ ) and the spanwise lo-  
 241 cation ( $Z$ ) (transverse ridges are dependent upon  $X$  and  $Y$ ).  
 242 The turbulent statistics just above a ridge are different from  
 243 those just above a free surface region. For the post geometry,  
 244 the statistics are also dependent on the streamwise location  
 245 ( $X$ ). For this reason, the statistics are calculated by temporal  
 246 averaging and ensemble averaging over all the posts or  
 247 ridges on the surface. In practice, the topological surface  
 248 features are very small (on the scale of microns), and engi-  
 249 neers are interested in the larger scale bulk properties of the  
 250 flow. In this paper, we present the  $X$ - $Z$  planar averaged mean  
 251 flow and Reynolds stress profiles as a function of the dis-  
 252 tance to the wall ( $Y$ ). The distinction between the planar  
 253 averaged statistics and the actual turbulent statistics is only  
 254 important at distances to the wall that are less than the gap  
 255 width. However, in that region this distinction is critical. Us-  
 256 ing the planar averaged mean velocity rather than the actual  
 257 (spatially varying) mean velocity to calculate the Reynolds

stresses produces erroneous results. This may be a particular  
 issue in experimental studies where the spatially varying  
 mean flow is very difficult to measure.

Two different ridge geometries and one post geometry  
 were studied at  $Re_\tau \approx 395$ . The planar averaged mean veloc-  
 ity profiles for those three cases as well as standard channel  
 flow are shown in Fig. 6. Spencer *et al.*<sup>38</sup> saw similar shifts  
 in peak velocity toward a hydrophobic wall in their investi-  
 gations. The post case, with its larger gap size (and much  
 larger free surface area percentage) shows the most slip on  
 the lower wall and the greatest mass flux. Because these  
 simulations have the same  $Re_\tau$  they are effectively operating  
 at the same pressure gradient. This shows that with a super-  
 hydrophobic surface, more mass can be moved through the  
 channel for the same effort. To show that the slip is actually  
 a function of the gap spacing (and not simply the free surface  
 area percentage), the two ridge cases have exactly the same  
 free surface area percentage and different gap spacings. The  
 smaller gap size ( $\square$ ) results in a smaller slip velocity on the  
 lower wall and less mass flux. To first order, it can be seen  
 that the additional mass flux produced by a superhydropho-  
 bic surface is roughly proportional to the gap size of that  
 surface. For this reason, very small (nanoscale) features may  
 be ineffective for drag reduction. Figure 7 shows the velocity

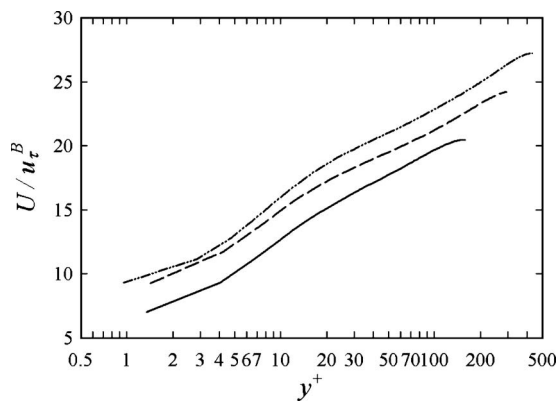


FIG. 11. A closer look at velocity profiles from Fig. 10, using the local friction velocity  $u_\tau^B$  to normalize the velocity and calculate  $y^+$ .

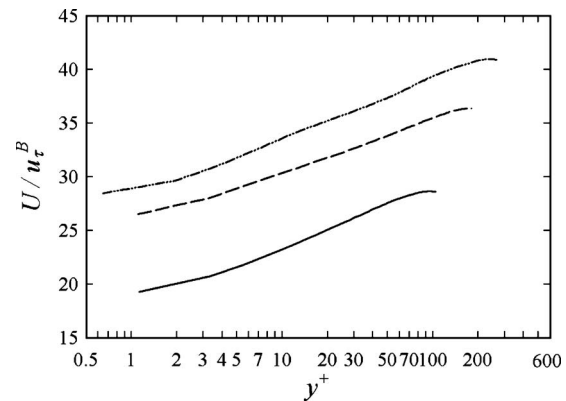


FIG. 13. A closer look at velocity profiles from Fig. 12, using the local friction velocity  $u_\tau^B$  to normalize the velocity and calculate  $y^+$ .

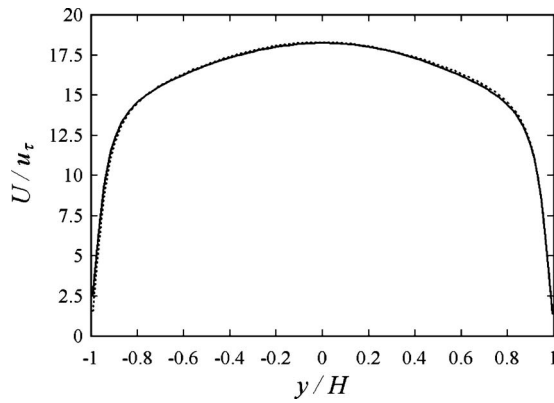


FIG. 14. Comparison of velocity profiles for transverse  $g/w=1$ ,  $w/H=g/H=0.18750$  ridges at  $Re_\tau \approx 180$  (—) with regular channel profile (···) shown for reference.

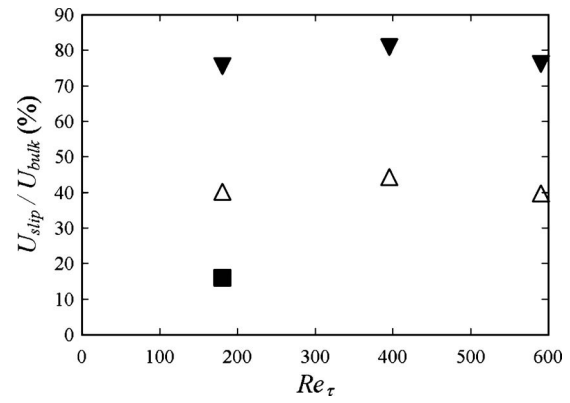


FIG. 16. Slip velocity as a percentage of bulk velocity for  $g/w=1$ ,  $w/H=g/H=0.18750$  ridges ( $\Delta$ ) and  $g/w=3$ ,  $w/H=0.09375$ , and  $g/H=0.28124$  posts ( $\nabla$ ) at  $Re_\tau \approx 180, 395$ , and  $590$ , as well as transverse  $g/w=1$ ,  $w/H=g/H=0.18750$  ridges ( $\blacksquare$ ). Note that the ridge spacing in wall units increases with increased  $Re_\tau$ .

profiles in wall units (based on the bottom wall). The effective slip velocity caused by the superhydrophobic surfaces is now quite apparent. To first order these surfaces shift the log-law upwards, but do not alter its slope.

The behavior of the mean flow as the Reynolds number increases to  $Re_\tau \approx 590$  is shown in Fig. 8. The same profile in wall units based on the superhydrophobic (bottom wall) friction velocity is shown in Fig. 9. Again, in this case, higher Reynolds number essentially implies that a higher pressure gradient is being applied to the same channel. As expected, this drives the fluid faster through the channel. The slip velocity, however, does not appear to be a strong function of the Reynolds number. This can be seen clearly in Fig. 16, when the slip velocity is normalized by the average velocity in the channel. As will be discussed later, it is possible that the  $Re_\tau \approx 180$  case is showing low Reynolds number effects and the two higher Reynolds number cases are more indicative of fully developed channel flow.

The velocity profiles for evenly spaced ridges at varying Reynolds numbers are shown in Fig. 10. The velocity in locally scaled wall units is shown in Fig. 11. The mean flow profiles for widely spaced posts at varying Reynolds numbers are shown in Fig. 12, while the velocity in locally scaled wall units is shown in Fig. 13. For both posts and ridges, the slip velocity is only mildly dependent on the Reynolds number for the higher Reynolds number cases. In the case of transverse ridges, it is not surprising that they admit a very small slip velocity at the superhydrophobic wall as seen in Figs. 14 and 15. The amount of slip admitted by transverse ridges may be reduced further if the interface were allowed to deflect, as this may lead to recirculation above the ridge gaps. Recirculation, along with streamline curvature, might affect a drag increase similar to what was shown in the work of Min and Kim<sup>25</sup> when transverse slip was considered. The slip velocity as a percentage of the bulk velocity versus the Reynolds number is shown in Fig. 16 for both the ridge and post cases. This figure confirms that the Reynolds number is not a strong factor in the observed dimensionless slip velocity of the superhydrophobic surface. This is important because it is likely that these surfaces will be used at much higher Reynolds numbers than we have computed here. The effective slip is an important parameter because it is directly related to the drag reduction. In our simulations, the pressure gradient is fixed, so that reduced drag on the superhydrophobic wall will lead to increased drag on the upper wall (because of the increased mass flow) and the same total drag in the channel. Figure 17 plots the slip velocity normalized by the bottom-wall friction velocity versus Reynolds number, and Fig. 18 plots the drag reduction on the lower wall versus

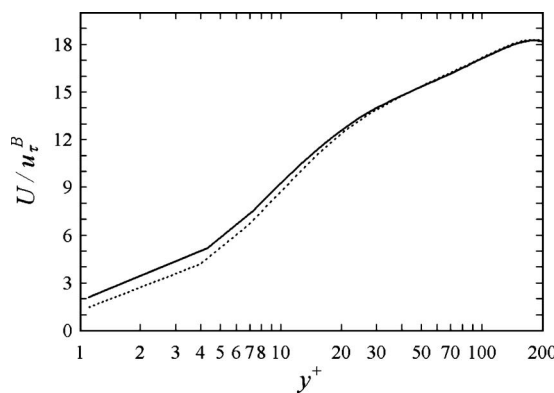


FIG. 15. A closer look at velocity profiles from Fig. 14, using the local friction velocity  $u_\tau^B$  to normalize the velocity and calculate  $y^+$ .

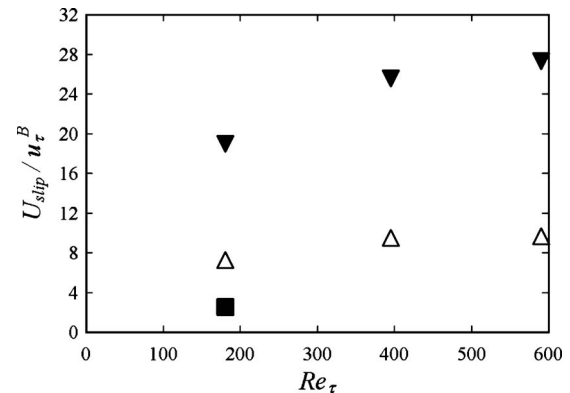


FIG. 17. Slip velocity normalized by bottom-wall friction velocity for the same geometries shown in Fig. 16.

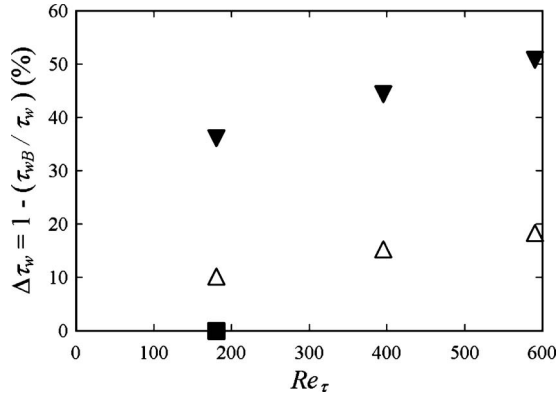


FIG. 18. Superhydrophobic surface shear stress reduction as a function of friction Reynolds number for the same geometries and Reynolds numbers reported in Fig. 16.

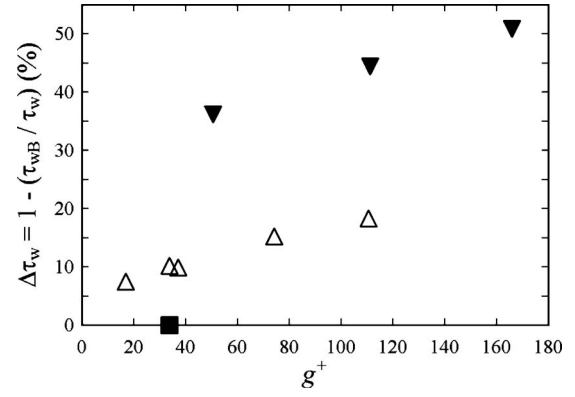


FIG. 20. Superhydrophobic surface shear stress reduction as a function of  $g^+$  for fixed  $w^+/g^+=1$  ridges ( $\Delta$ ), posts ( $\blacktriangledown$ ), and transverse ridges ( $\blacksquare$ ). Transverse ridges exhibit near-zero shear stress reduction.

the Reynolds number (for the ridge and post cases). These figures show that the percent drag reduction varies with Reynolds number. It is important to note that increasing the Reynolds number while keeping  $g/H$  and  $w/H$  fixed increases the microfeature spacing in wall units ( $w^+$  and  $g^+$ ). Thus even though all of the simulations in Figs. 10–18 are performed at the same physical post or ridge width and spacing, their dimensions in wall units increases substantially with increasing Reynolds number. Transverse ridges exhibit negligible shear stress reduction and closely resemble the regular channel results. This adds further evidence that feature spacing, and perhaps feature alignment, play a key role in surface performance. We hypothesize that feature spacing in wall units, and not Reynolds number, is the critical criteria for characterizing superhydrophobic performance in turbulent flows. To test this hypothesis, two ridge geometries were simulated at different physical spacings and Reynolds numbers, but with nearly identical ridge spacing and width in wall units. The velocity profiles from these two simulations are shown in Fig. 19. When normalized by the friction velocity, the profiles collapse. Thus neither increasing the Reynolds number or reducing the physical gap size had an effect on the performance of the superhydrophobic surface. This confirms

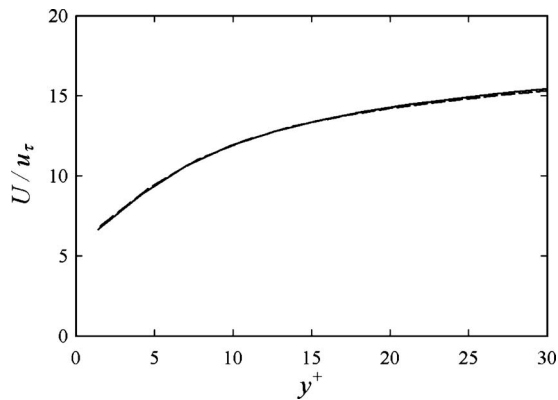


FIG. 19. Near-wall velocity profiles for  $w^+=g^+=33.75$  ridges ( $w/H=g/H=0.1875$ ) at  $Re_\tau \approx 180$  (—) and  $w^+=g^+=37.031$  ridges ( $w/H=g/H=0.09375$ ) at  $Re_\tau \approx 395$  (---). The profiles lie atop one another, indicating the increase in Reynolds number may not affect the superhydrophobic surface performance.

our hypothesis that it is the gap spacing in wall units that dictates drag reduction. This suggests that it might be more appropriate to plot drag reduction as a function of the feature spacing in wall units  $w^+$  rather than as a function of Reynolds number. Figure 20 shows superhydrophobic surface shear stress reduction as a function of  $g^+$  for fixed  $w^+/g^+=1$ . A nearly linear growth in drag reduction is observed for both the superhydrophobic ridges and posts. A deviation from this trend will likely be observed at low values of feature spacing if the value of drag reduction in laminar flow is to be recovered. Note that  $\tau_w$  is the wall shear stress present in a comparable regular wall channel.

#### IV. REYNOLDS STRESSES

Figures 21–24 show the normalized planar averaged Reynolds stresses for all the cases at  $Re_\tau \approx 395$ . The results suggest that mean shear is still the primary influence on the turbulence levels. Reduced shear at the superhydrophobic surface results in reduced turbulent production and lower turbulence levels for all the shear stresses. The magnitude of the turbulence drop is closely related to the magnitude of the shear reduction that occurred due to the slip on the surface. Similarly, on the regular (upper) wall the shear increases

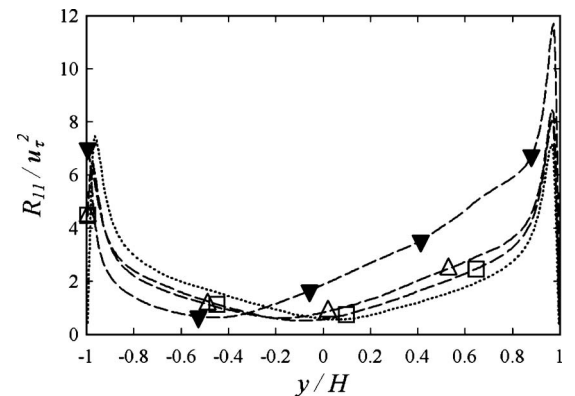
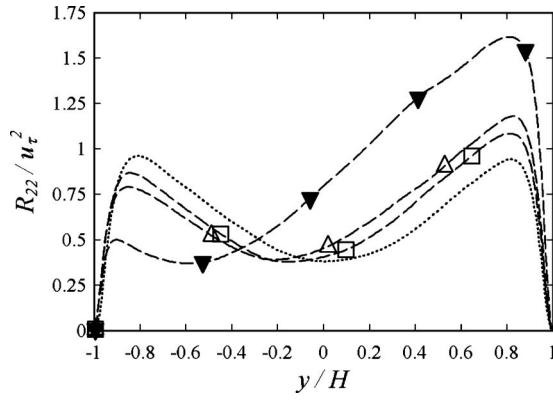
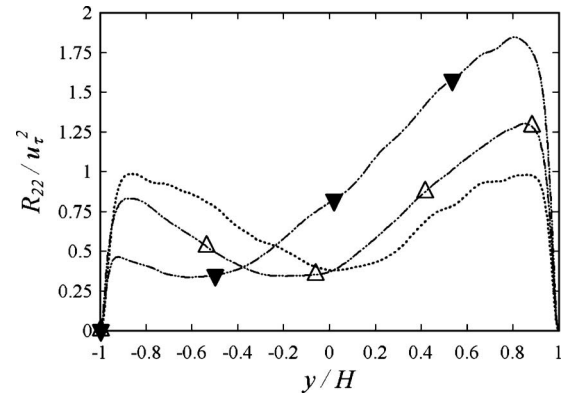
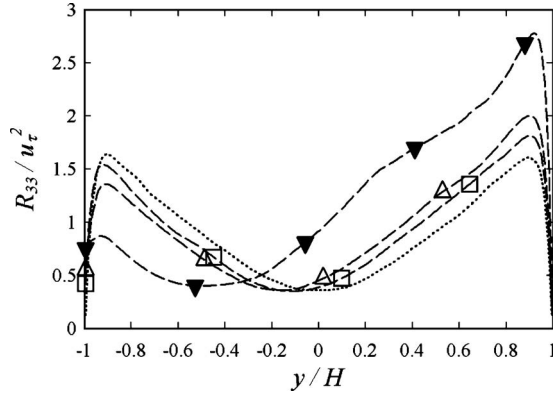
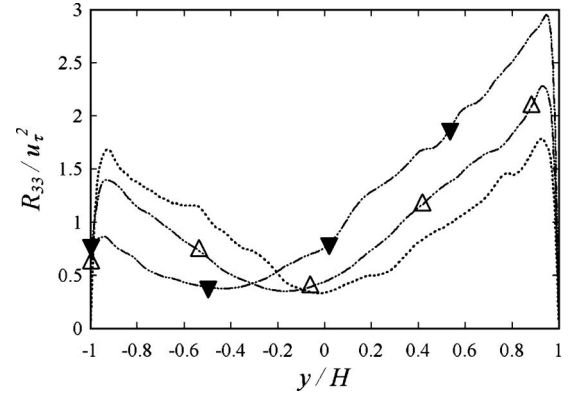
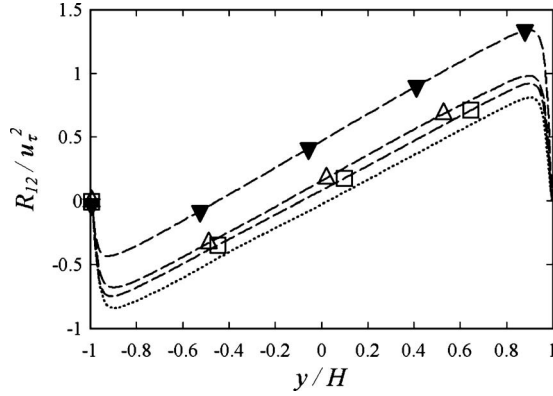
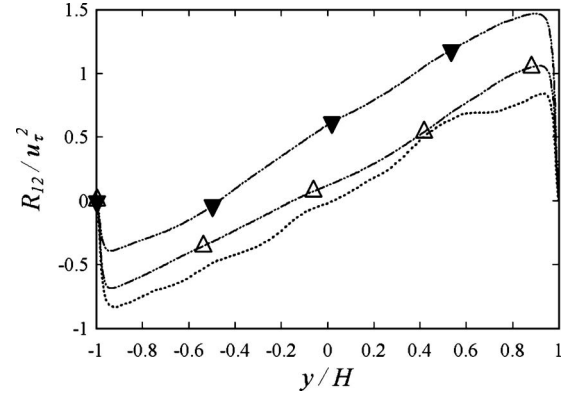
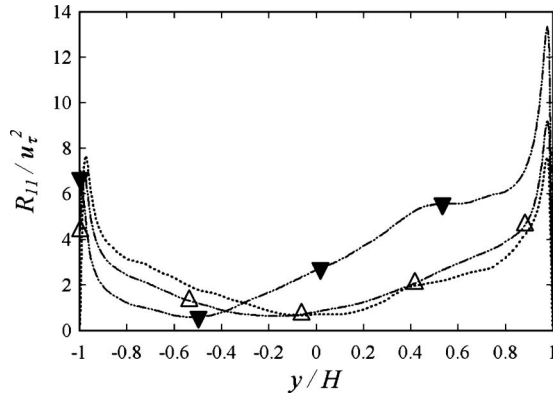
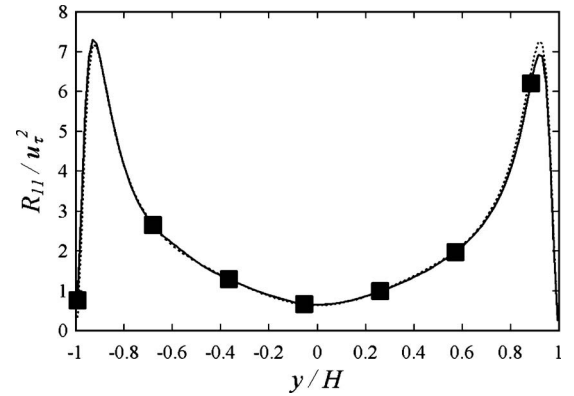


FIG. 21.  $Re_\tau \approx 395$ .  $R_{11}$  profiles from simulations with  $w^+=g^+=37.031$  ( $\square$ ) and  $w^+=g^+=74.062$  ( $\Delta$ ) ridges, as well as  $w^+=37.031$ ,  $g^+=111.09$  ( $\blacktriangledown$ ) posts. Regular channel profile ( $\cdots$ ) shown for reference. Note that symbols are used to identify curves, and do not reflect data point locations.

FIG. 22.  $Re_\tau \approx 395$ .  $R_{22}$  profiles for the same geometries reported in Fig. 21.FIG. 26.  $Re_\tau \approx 590$ .  $R_{22}$  profiles for the same geometries reported in Fig. 25.FIG. 23.  $Re_\tau \approx 395$ .  $R_{33}$  profiles for the same geometries reported in Fig. 21.FIG. 27.  $Re_\tau \approx 395$ .  $R_{33}$  profiles for the same geometries reported in Fig. 25.FIG. 24.  $Re_\tau \approx 395$ .  $R_{12}$  profiles for the same geometries reported in Fig. 21.FIG. 28.  $Re_\tau \approx 590$ .  $R_{12}$  profiles for the same geometries reported in Fig. 25.FIG. 25.  $Re_\tau \approx 590$ .  $R_{11}$  profiles from simulations with  $w^+ = g^+ = 110.62$  ( $\Delta$ ) ridges, as well as  $w^+ = 55.313$  and  $g^+ = 165.94$  ( $\blacktriangledown$ ) posts. Regular channel profile ( $\cdots$ ) shown for reference.FIG. 29.  $Re_\tau \approx 180$ .  $R_{11}$  profiles from simulations with transverse  $g/w = 1$ ,  $w/H = g/H = 0.1875$  50 ridges ( $\blacksquare$ ). Regular channel profile ( $\cdots$ ) shown for reference.



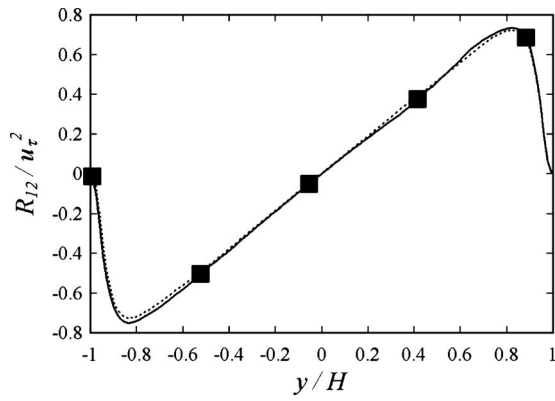
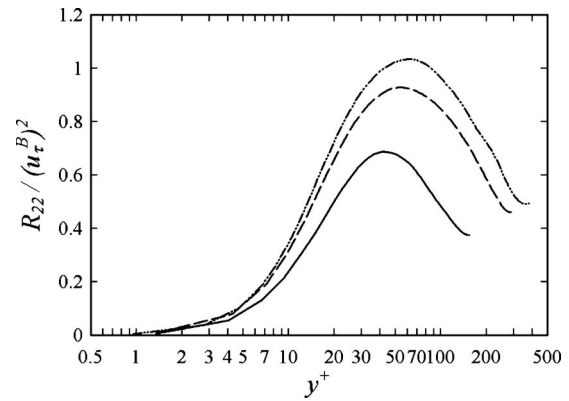
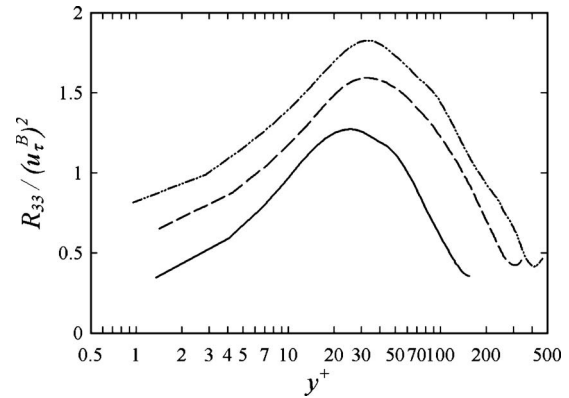
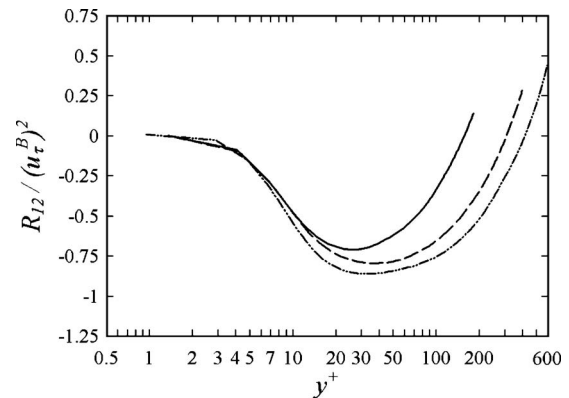
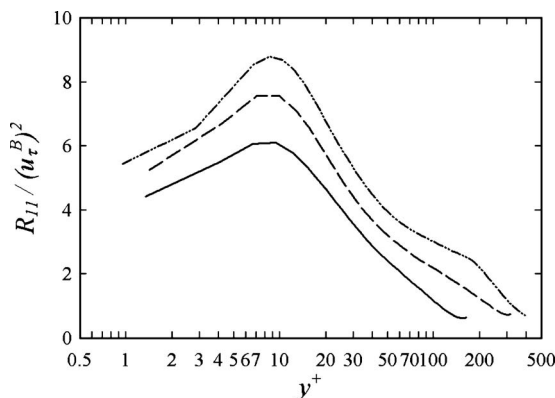
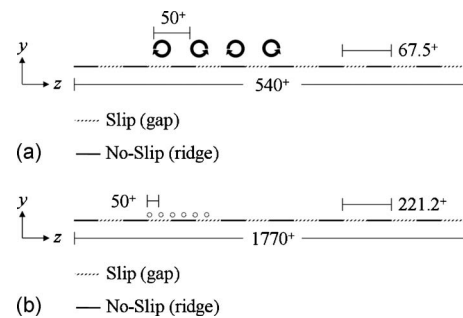
FIG. 30.  $Re_\tau \approx 180$ .  $R_{12}$  profiles for the same geometries reported in Fig. 29.FIG. 32. Comparison of  $R_{22}$  profiles for the same cases discussed in Fig. 31.FIG. 33. Comparison of  $R_{33}$  profiles for the same cases discussed in Fig. 31.FIG. 34. Comparison of  $R_{12}$  profiles for the same cases discussed in Fig. 34.FIG. 31. Comparison of  $R_{11}$  profiles for  $g/w=1$ ,  $w/H=g/H=0.1875$  ridges across the three Reynolds numbers investigated:  $Re_\tau \approx 180$  (—) with  $w^+=g^+=33.75$ ,  $Re_\tau \approx 395$  (---) with  $w^+=g^+=74.062$ , and  $Re_\tau \approx 590$  (— · —) with  $w^+=g^+=110.62$ .

FIG. 35. Schematic representing pairs of counter-rotating vortices for channel flow over ridges at two different Reynolds numbers.

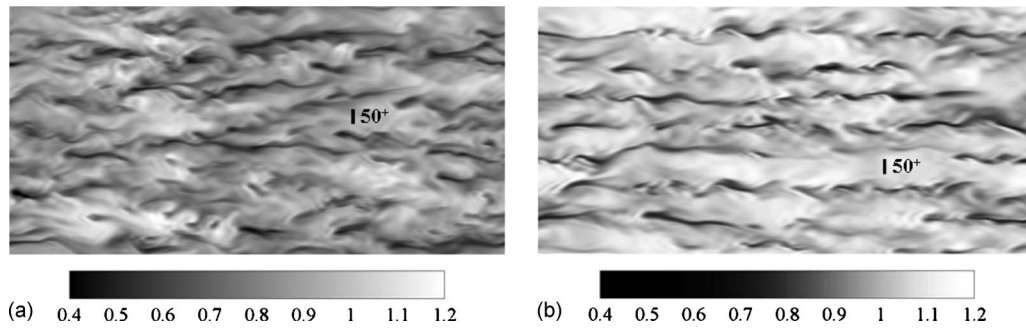


FIG. 36.  $Re_\tau \approx 395$ . Instantaneous streamwise velocity ( $U$ ) contour slices ( $XZ$ ), normalized by  $U_{\text{bulk}}$ , for a regular channel and one with  $w^+ = 37.031$ ,  $g^+ = 111.09$  posts. The slice in (a) is taken at  $y^+ \approx 44$ , while the slice in (b) is taken at  $y^+ \approx 22$ . Feature sizes and shapes are roughly equivalent.

the amount of energy dissipation near the surface (by removing the surface-parallel viscous damping of the turbulence). For this reason, the flow does not relaminarize on the superhydrophobic surface when local shear arguments alone might suggest it should. Note that the unsmooth regions present in the  $Re_\tau \approx 590$  post Reynolds stress profiles are a result of insufficient statistical averaging in time and are not indicative of any physical phenomena. It is of no surprise that the Reynolds stress profiles for transverse ridges are nearly identical to those for the regular channel as seen in Figs. 29 and 30. Unlike their streamwise counterparts, the transverse ridges do not appear to affect the location or intensity of turbulent structures in the flow.

The Reynolds stresses are plotted in wall coordinates in Figs. 31–34 for  $g/w = 1$ ,  $w/H = g/H = 0.187$  50 ridges at  $Re_\tau \approx 180$ ,  $Re_\tau \approx 395$ , and  $Re_\tau \approx 590$ . The local (lower wall) friction velocity is used in the normalization and in the calculation of  $y^+$ . While these figures appear to show Reynolds number variation, it is hypothesized that they may be revealing variation with gap and feature widths  $g^+$  and  $w^+$ .

## V. STRUCTURES

The mean flow profiles and Reynolds stresses imply that the superhydrophobic surface does not alter the fundamental structures of the turbulent boundary layer. The near wall behavior of the turbulent shear stress ( $R_{12}$ ) continues to collapse on wall shear units. The log-law remains intact (though shifted upwards) for the mean flow. This section will look closely at the streaks (and streamwise vortices) associated

with boundary layer flows, and will investigate how they are affected by the regular array of microfeatures on the superhydrophobic surface.

Streaks (pairs of counter-rotating vortices) have an average spanwise spacing of roughly  $100^+$  units.<sup>40</sup> This means that as the Reynolds number is increased ( $w/H$  and  $g/H$  are held fixed), the streaks (and their associated streamwise vortices) become smaller. Figure 35(a) depicts the size and shape of vortices for a channel with evenly spaced ridges ( $w/H = 0.125$ ) at  $Re_\tau \approx 180$  on a cross section looking down the channel. The tops of the ridges are shown with a solid black line and the tops of each free surface are shown with a dashed line. The counter-rotating streamwise vortices that form the low-speed and high-speed streaks are shown residing just above the surface. For this particular case, the ridge spacing and the streak spacing are nearly equal. Having the ridge spacing equal to the streak spacing means that the ridges have the potential to act such as riblets (see Ref. 41). Riblets reduce drag by damping the spanwise motion of streamwise vortices. This could be a reason (in addition to low Reynolds number effects) why the  $Re_\tau \approx 180$  simulations behave slightly differently from the higher Reynolds number simulations. We note however, that the posts have little ability to control spanwise streak motion yet they too show slight differences at  $Re_\tau \approx 180$ .

Figure 35(b) shows the same surface topology at the higher Reynolds number,  $Re_\tau \approx 590$ . The vortices are now much smaller than the ridges and free surface regions (gaps), and the vortices are also closer to the superhydrophobic surface. It is unlikely now that the streaks and ridges (or posts)

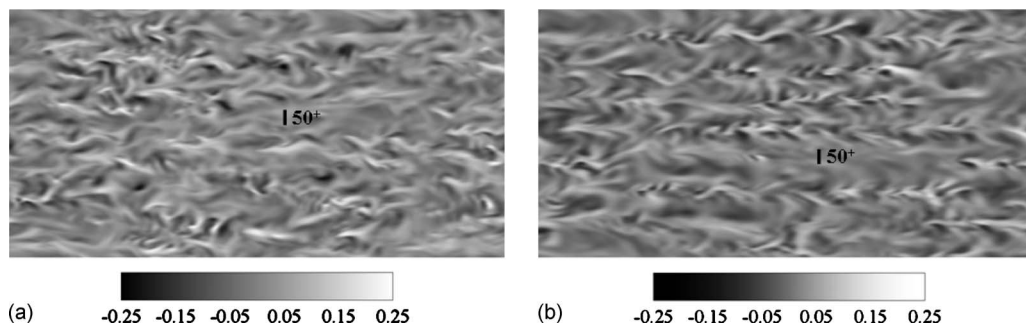


FIG. 37.  $Re_\tau \approx 395$ . Instantaneous vertical ( $V$ ) velocity contour slices ( $XZ$ ), normalized by  $U_{\text{bulk}}$ , similar to those found in Fig. 36, for the same geometries, taken at the same  $y^+$  locations.

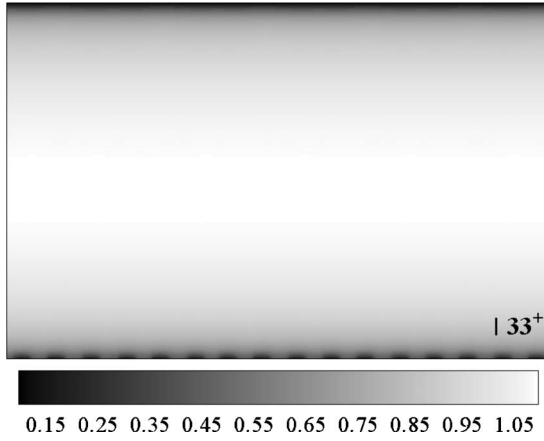


FIG. 38.  $Re_\tau \approx 180$ . Time-averaged streamwise ( $U$ ) velocity contour slice ( $YZ$ , looking downstream), normalized by  $U_{\text{bulk}}$ , for  $w^+ = g^+ = 33.75$  streamwise ridges. Note that the presence of the ridges alters the mean flow up until  $y^+ \approx 10-15$ .

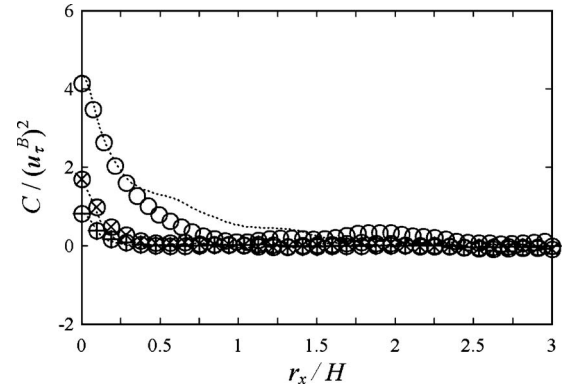


FIG. 39.  $Re_\tau \approx 395$ . A comparison of velocity correlation profiles in the streamwise ( $X$ ) direction at  $y^+ \approx 44$  obtained from a regular channel ( $\circ$   $uu$ ,  $\oplus$   $vv$ , and  $\otimes$   $ww$ ) and  $w^+ = 37.031$  and  $g^+ = 111.09$  posts at  $y^+ \approx 22$  ( $\cdots$ ). Note that these are the same  $y^+$  locations shown in Figs. 36 and 37.

changing the nature of the near-wall turbulent structures. Note that the velocities were normalized by the bulk streamwise velocity in order to better accentuate the turbulent features present in the flow. The bottom wall friction velocity ( $u_\tau^B$ ) was *not* used for normalization as the value of  $u_\tau^B$  differs greatly between regular channels and those with ridges or posts.

Figure 38 shows time-averaged streamwise velocity ( $U$ ) contours over  $w^+ = g^+ = 33.75$  streamwise ridges on the bottom wall at  $Re_\tau \approx 180$ . The difference between flow over the gaps (lighter regions with higher velocity) and flow over the ridges themselves (darker regions with near-zero velocity) is clearly seen. The presence of the ridges appears to affect the mean flow in the channel up to a height of  $y^+ \approx 10-15$ , and the smooth transition between shear-free and no-slip regions is observed. Statistics taken over the ridge will resemble those for a “normal” no-slip wall, and similarly statistics taken over a gap will be similar to those found above a “normal” free surface. Superhydrophobic features affect the near-wall region up to a distance less than or equal to the feature spacing in wall units ( $g^+$ ).

Figures 39 and 40 compare velocity correlations in  $X$  and  $Z$  for a regular wall channel and  $w^+ = 37.031$ ,  $g^+ = 111.09$  post channel both at  $Re_\tau \approx 395$ . For the regular

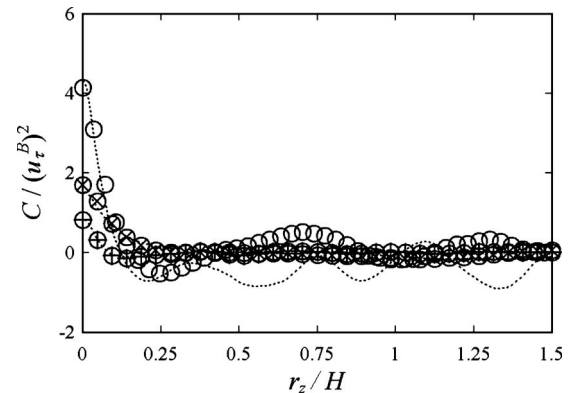


FIG. 40.  $Re_\tau \approx 395$ . A comparison of velocity correlation profiles in the spanwise ( $Z$ ) direction at the same  $y^+$  locations, as shown in Figs. 36 and 37. See Fig. 39 for symbol key.

are acting such as riblets. The Min and Kim simulations,<sup>25</sup> where a slip boundary condition is assumed for the whole lower surface, would be equivalent to the opposite situation where the ridges are extremely small compared to the near wall structures. The behavior of the mean flow and Reynolds stresses suggests that very similar near-surface structures are likely to exist adjacent to the superhydrophobic surface. This is confirmed by Fig. 36 which shows a slice of the streamwise velocity, normalized by the bulk streamwise velocity, which is parallel to and just above the superhydrophobic surface, and Fig. 37 which shows the vertical velocity (also normalized by the bulk streamwise velocity) in the same plane. The top picture is a regular channel flow (at  $Re_\tau \approx 395$ ) and the bottom slice is from the widely spaced post case (at the same Reynolds number). The contour levels are identical in both pictures, so that it is clear that both the magnitude and size of the streaks are very similar in both flows. A bar corresponding to 50<sup>+</sup> wall units has been added to compare the relative sizes of features present in the flow. The slices are taken at  $y$ -positions where the local shear is the same. In the case of the regular channel, the slice is at  $y^+ \approx 44$  and in the case of the posts this level of shear does not occur until one is closer to the surface (at  $y^+ \approx 22$ ). The location with the same mean shear was chosen because Lee *et al.*<sup>42</sup> suggest that shear (not wall locality) is the driving mechanism in streak formation. The shift in position roughly corresponds to the slip-length in wall units. For the widely spaced post case in both Figs. 36 and 37, the turbulent structures are not closely related to the post positions, although the structures shown in Fig. 36(b) appear to remain aligned down the length of the channel while in (a), which shows the regular wall channel, the streaks intersect more and are generally less structured. The fact that the post case has only 6.25% of the surface occupied by a solid wall indicates that boundary layer turbulent structures are dominated by the mean shear and the zero vertical velocity (no penetration) boundary condition. The tangential boundary condition (slip or no-slip) appears to have a very significant affect on the overall drag without dramatically



wall channel, correlations were calculated at  $y^+ \approx 44$ . For  $w^+ = 37.031$ ,  $g^+ = 111.09$  posts, correlations were computed at  $y^+ \approx 22$ . The correlations match well for moderate  $r_x$  and  $r_z$  which further supports the hypothesis that shear may be primarily responsible for streak formation. Furthermore, the correlations show the computational domain is both wide and long enough even with significant shear free surface present on the lower wall. The unsmooth nature of the streamwise velocity correlation in the spanwise direction (seen in Fig. 40) may be due to the presence of streaks and the lack of temporal averaging, as the behavior roughly responds to the spanwise streak spacing. Note that the size of the fluctuations does not correspond to the post size or spacing, and would most likely average to zero over time.

## VI. CONCLUDING REMARKS

Superhydrophobic surfaces produce changes in turbulent channel flow through several different mechanisms. They allow low average slip velocities (along the surface) which approach the channel's bulk velocity. The shear stress at the superhydrophobic surface (which can be directly related to drag reduction) is significantly reduced when compared with regular channel flow. The shear stress reduction (near 10%) found for  $w/H = g/H = 0.1875$  ridges at  $Re_\tau \approx 180$  closely matches the drag reduction reported in the experiments of Daniello *et al.*<sup>22,31</sup> The superhydrophobic surfaces alter the symmetry, peak magnitude, and peak locations of Reynolds stresses, largely in keeping with the redistribution of mean shear throughout the channel.

For all geometries investigated, and at all Reynolds numbers, the widely spaced posts outperformed the ridges by supporting a higher slip velocity and exhibiting a greater decrease in wall shear stress. It appears as though the dimensionless slip velocity is independent of the Reynolds number (for fixed  $g^+$  and  $w^+$ ). Many of the results appear to have Reynolds number dependence when  $w/H$  and  $g/H$  are held fixed. The indications are, however, that when scaled appropriately (on  $g^+$  and  $w^+$ ) the flow behavior may be independent of Reynolds number.

Turbulent structures in the channel are shifted but otherwise largely unaffected by the superhydrophobic surface. Examination of scaled  $R_{12}$  profiles, and of instantaneous streamwise and vertical velocity fields indicates that the turbulent structures remain intact, and are simply shifted toward the superhydrophobic surface. This is useful, as it means the existing theory and understanding of turbulent structures still applies to turbulent channel flow over superhydrophobic surfaces, and simply requires the turbulent structure locations to be modified. An understanding of this shift will allow engineers to model and predict the performance of superhydrophobic surfaces.

## ACKNOWLEDGMENTS

The authors would like to thank the Office of Naval Research for support of this research under Grant No. N00014-06-1-0497.

- <sup>1</sup>D. Öner and T. J. McCarthy, "Ultrahydrophobic surfaces. Effects of topography length scales on wettability," *Langmuir* **16**, 7777 (2000).
- <sup>2</sup>W. Chen, A. Y. Fadeev, M. C. Hsieh, D. Öner, J. Youngblood, and T. J. McCarthy, "Ultrahydrophobic and ultralyophobic surfaces: Some comments and examples," *Langmuir* **15**, 3395 (1999).
- <sup>3</sup>W. Barthlott and C. Neinhuis, "Purity of the sacred lotus, or escape from contamination in biological surfaces," *Planta* **202**, 1 (1997).
- <sup>4</sup>K. Watanabe, H. Yanuar, and H. Udagawa, "Drag reduction of Newtonian fluid in a circular pipe with highly water-repellant wall," *J. Fluid Mech.* **381**, 225 (1999).
- <sup>5</sup>K. Watanabe and T. Akino, "Drag reduction in laminar flow between two vertical coaxial cylinders," *ASME J. Fluids Eng.* **121**, 541 (1999).
- <sup>6</sup>K. Watanabe, H. Yanuar, O. Katsutoshi, and H. Mizunuma, "Drag-reduction in flow through square and rectangular ducts with highly water repellent walls," Proceedings of the Second ASME Fluids Engineering Conference, 1996, Vol. 237, p. 115–119.
- <sup>7</sup>K. Watanabe, T. Takayama, S. Ogata, and S. Isozaki, "Flow between two coaxial rotating cylinders with a highly water-repellent wall," *AIChE J.* **49**, 1956 (2003).
- <sup>8</sup>T. Jun and X. Qunji, "Plate drag-reduction with low surface-energy coating in a water tunnel," *Chin. Sci. Bull.* **42**, 307 (1997).
- <sup>9</sup>J. Ou, J. B. Perot, and J. P. Rothstein, "Laminar drag reduction in microchannels using superhydrophobic surfaces," *Phys. Fluids* **16**, 4635 (2004).
- <sup>10</sup>J. Ou and J. Rothstein, "Direct velocity measurements of the flow past drag-reducing ultrahydrophobic surfaces," *Phys. Fluids* **17**, 103606 (2005).
- <sup>11</sup>P. Joseph, C. Cottin-Bizonne, J. M. Benot, C. Ybert, C. Journet, P. Tabeling, and L. Bocquet, "Slippage of water past superhydrophobic carbon nanotube forests in microchannels," *Phys. Rev. Lett.* **97**, 156104 (2006).
- <sup>12</sup>D. Maynes and B. W. Webb, "Fully developed electro-osmotic heat transfer in microchannels," *Int. J. Heat Mass Transfer* **46**, 1359 (2003).
- <sup>13</sup>J. R. Philip, "Flows satisfying mixed no-slip and no-shear conditions," *Z. Angew. Math. Phys.* **23**, 353 (1972).
- <sup>14</sup>J. R. Philip, "Integral properties of flows satisfying mixed no-slip and no-shear conditions," *Z. Angew. Math. Phys.* **23**, 960 (1972).
- <sup>15</sup>J. Lauga and H. Stone, "Effective slip in pressure-driven stokes flow," *J. Fluid Mech.* **489**, 55 (2003).
- <sup>16</sup>T. D. Gordon and T. J. McCarthy, "Drag-reduction and slip: An investigation of size scale and hydrophobicity effects," Proceedings of the ASME Fluids Engineering Division, 2000, Vol. 253, p. 367.
- <sup>17</sup>S. Gogte, P. Vorobieff, R. Truesdell, A. Mammoli, F. van Swol, P. Shah, and C. J. Brinker, "Effective slip on textured superhydrophobic surfaces," *Phys. Fluids* **17**, 051701 (2005).
- <sup>18</sup>Y. Murai, H. Oiwa, and Y. Takeda, "Frictional drag reduction in bubbly Couette–Taylor flow," *Phys. Fluids* **20**, 034101 (2008).
- <sup>19</sup>J. Davies, D. Maynes, B. W. Webb, and B. Woolford, "Laminar flow in a microchannel with superhydrophobic walls exhibiting transverse ribs," *Phys. Fluids* **18**, 087110 (2006).
- <sup>20</sup>S. Hahn, J. Je, and H. Choi, "Direct numerical simulation of turbulent channel flow with permeable walls," *J. Fluid Mech.* **450**, 259 (2002).
- <sup>21</sup>J. W. G. Tyrrell and P. Attard, "Images of nanobubbles on hydrophobic surfaces and their interactions," *Phys. Rev. Lett.* **87**, 176104 (2001).
- <sup>22</sup>R. J. Daniello, N. E. Waterhouse, and J. P. Rothstein, "Drag reduction in turbulent flows over superhydrophobic surfaces," *Phys. Fluids* **21**, 085103 (2009).
- <sup>23</sup>B. L. Woolford, "Laminar and turbulent flow of a liquid through channels with superhydrophobic walls exhibiting alternating ribs and cavities," Ph.D. thesis, The University of Massachusetts Amherst, 2009.
- <sup>24</sup>K. Fukagata, N. Kasagi, and P. Koumoutsakos, "A theoretical prediction of friction drag in turbulent flow by superhydrophobic surfaces," *Phys. Fluids* **18**, 051703 (2006).
- <sup>25</sup>T. Min and J. Kim, "Effects of hydrophobic surface on skin-friction drag," *Phys. Fluids* **16**, L55 (2004).
- <sup>26</sup>T. Min and J. Kim, "Effects of hydrophobic surface on stability and transition," *Phys. Fluids* **17**, 108106 (2005).
- <sup>27</sup>M. B. Martell, J. B. Perot, and J. P. Rothstein, "Direct numerical simulations of turbulent flows over superhydrophobic surfaces," *J. Fluid Mech.* **620**, 31 (2009).
- <sup>28</sup>C. Ybert, C. Barentin, and C. Cottin-Bizonne, "Achieving large slip with superhydrophobic surfaces: Scaling laws for generic geometries," *Phys. Fluids* **19**, 123601 (2007).



- 648<sup>29</sup>M. B. Martell, "Simulations of turbulence over superhydrophobic sur- 666  
 649 faces," M.S. thesis, The University of Massachusetts Amherst, 2009. 667
- AQ: 650<sup>30</sup>R. Moser, J. Kim, and N. Mansour, "Direct numerical simulation of tur- 668  
 #5 651 bulent channel flow up to  $Re_x=590$ ," *Phys. Fluids* **11**, 943 (1999). 669  
 652<sup>31</sup>R. J. Daniello, "Drag reduction in turbulent flows over micropatterned 670  
 653 superhydrophobic surfaces," M.S. thesis, The University of Massachusetts 671  
 654 Amherst, 2009. 672  
 655<sup>32</sup>J. B. Perot, "An analysis of the fractional step method," *J. Comput. Phys.* 673  
 656 **108**, 51 (1993). 674  
 657<sup>33</sup>J. B. Perot, "Conservation properties of unstructured staggered mesh 675  
 658 schemes," *J. Comput. Phys.* **159**, 58 (2000). 676  
 659<sup>34</sup>R. Mittal and P. Moin, "Suitability of upwind-biased finite difference 677  
 AQ: 660 schemes for large-eddy simulation of turbulent flows," *AIAA J.* **35**, 1415 678  
 #6 661 (1997). 679  
 662<sup>35</sup>X. Zhang, D. Schmidt, and J. B. Perot, "Accuracy and conservation prop- 680  
 663 erties of a three-dimensional staggered mesh scheme," *J. Comput. Phys.* 681  
 664 **175**, 764 (2002). 682  
 665<sup>36</sup>M. Nilsson, Exploring fundamental turbulent physics using direct 683  
 numerical simulations, M.S. thesis, The University of Massachusetts, Am-  
 herst, 2008.
- <sup>37</sup>J. B. Perot and J. Gadebusch, "A stress transport equation model for simu-  
 lating turbulence at any mesh resolution," *Theor. Comput. Fluid Dyn.* **23**,  
 271 (2009).
- <sup>38</sup>N. B. Spencer, L. L. Lee, R. N. Parthasarathy, and D. V. Papavassiliou,  
 "Turbulence structure for plane Poiseuille-Couette flow and implications  
 for drag reduction over surfaces with slip," *Can. J. Chem. Eng.* **87**, 38  
 (2009).
- <sup>39</sup>J. B. Perot and P. Moin, "Shear-free turbulent boundary layers. Part 1.  
 Physical insights into near-wall turbulence," *J. Fluid Mech.* **295**, 199  
 (1995).
- <sup>40</sup>J. Kim, P. Moin, and R. Moser, "Turbulence statistics in fully developed  
 channel flow at low Reynolds number," *J. Fluid Mech.* **177**, 133 (1987).
- <sup>41</sup>H. Choi, P. Moin, and J. Kim, "Direct numerical simulation of turbulent  
 flow over riblets," *J. Fluid Mech.* **255**, 503 (1993).
- <sup>42</sup>M. J. Lee, J. Kim, and P. Moin, "Structure of turbulence at high shear  
 rate," *J. Fluid Mech.* **216**, 561 (1990).

**AUTHOR QUERIES — 038005PHF**

- #1 Au: Please spell out “MPI” if possible.
- #2 Au: Please supply variables in box symbol if there is any throughout.
- #3 Author: Please verify page number in Ref.1
- #4 Au: Please verify page number in Ref. 10.
- #5 Au: Please verify year in Ref. 30.
- #6 Au: Please verify year in Ref. 34.